New Journal of Physics
The open access journal at the forefront of physics

Deutsche Physikalische Gesellschaft DPG IOP Institute of Physics

PAPER • OPEN ACCESS

One-dimensional quantum magnetism in the anhydrous alum $KTi(SO_4)_2$

To cite this article: GJ Nilsen *et al* 2015 *New J. Phys.* **17** 113035

New Journal of Physics
The open access journal at the forefront of physics

Deutsche Physikalische Gesellschaft DPG
IOP Institute of Physics

Published in partnership with: Deutsche Physikalische Gesellschaft and the Institute of Physics

OPEN ACCESS

RECEIVED
27 July 2015

REVISED
28 September 2015

ACCEPTED FOR PUBLICATION
14 October 2015

PUBLISHED
16 November 2015

PAPER

One-dimensional quantum magnetism in the anhydrous alum $KTi(SO_4)_2$

GJ Nilsen[1,2], A Raja[2], AA Tsirlin[3,4], H Mutka[1], D Kasinathan[5], C Ritter[1] and HM Rønnow[2]

[1] Institut Laue-Langevin, 71 avenue des Martyrs, F-38042 Grenoble, France
[2] Laboratory for Quantum Magnetism, ICMP, Ecole Polytchnique Fédérale de Lausanne (EPFL), Switzerland
[3] Experimental Physics VI, Center for Electronic Correlations and Magnetism, Institute of Physics, University of Augsburg, D-86135 Augsburg, Germany
[4] National Institute of Chemical Physics and Biophysics, 12618 Tallinn, Estonia
[5] Max-Planck Institute for Chemical Physics of Solids, D-01187 Dresden, Germany

E-mail: nilsen@ill.fr

Keywords: Heisenberg chain, neutron scattering, quantum magnetism

Supplementary material for this article is available online

Abstract

The anhydrous alum $KTi(SO_4)_2$, where the Ti^{3+} (d^1, $S = 1/2$) ions form an anisotropic triangular lattice, has been prepared by a new hydrothermal route and characterized by magnetic susceptibility and neutron scattering measurements. Contrary to expectations, fits to the magnetic susceptibility indicate that the spins are isotropic (i.e. Heisenberg) and that the frustrating couplings are weak; indeed, the system is well modelled by nearly isolated chains. The inelastic neutron scattering data furthermore shows excellent agreement with an exact theoretical calculation for the one-dimensional spinon continuum. The unexpected magnetic properties of $KTi(SO_4)_2$ are explained in the light of density functional calculations, which reveal an unusual orbital ground state for the Ti^{3+} ion.

1. Introduction

Considered a cornerstone of quantum many-body physics for many decades [1], the antiferromagnetic $S = 1/2$ Heisenberg chain model (AQHC) continues to attract experimental and theoretical attention. This enduring appeal can be traced back to the model's richness, as well as its exact solvability. In zero magnetic field, the celebrated Bethe ansatz solution [2, 3] for the ground state is an entangled singlet characterized by algebraically decaying spin–spin correlations. Its excitations are $S = 1/2$ quasi-particles known as spinons [4, 5], which may be pictured as propagating domain walls arising from spin flips; because each flip produces an even number of spinons, they are observed in continua when using experimental techniques like inelastic neutron scattering. The recent availability of, on the one hand, large single crystals of systems which approximate the AQHC, and on the other, accurate calculations for the two and four-spinon dynamical scattering functions [6], has lead to several detailed neutron scattering measurements of spinon continua. Highlights include studies on $SrCuO_2$ [7], $Cu(SO_4) \cdot 5(H_2O)$ [8], and $KCuF_3$ [9], where careful data treatment and analysis permit a quantitative comparison with theory. In parallel with these works, there has also been considerable interest in the effect of perturbations on the AQHC, particularly relating to quantum criticality [10, 11] and geometric frustration. Regarding the latter, the most commonly considered model is the $S = 1/2$ Heisenberg anisotropic triangular lattice (QHAT), where intra- and interchain couplings generate a network of isosceles triangles [12–14] (figure 1). Perhaps the best known realizations of this model are found in the family of Cs_2CuX_4 (X = Cl, Br) materials [15–19]. In Cs_2CuCl_4, where the ratio of the intrachain to interchain coupling $J/J' \simeq 3$, neutron scattering has revealed the coexistence of a spinon continuum with a bound state induced by the interchain coupling [17, 18], as well as incommensurate spiral order at low temperatures [16].

Nearly twenty years ago, Bramwell *et al* proposed the anhydrous alums $AM(SO_4)_2$ (A = K, Rb, M = Ti, Fe) as an alternative set of compounds to represent both the anisotropic and isotropic ($J = J'$) triangular lattice models [21]. Among these, $KTi(SO_4)_2$ is the only compound which realizes the quantum limit $S = 1/2$, in this case

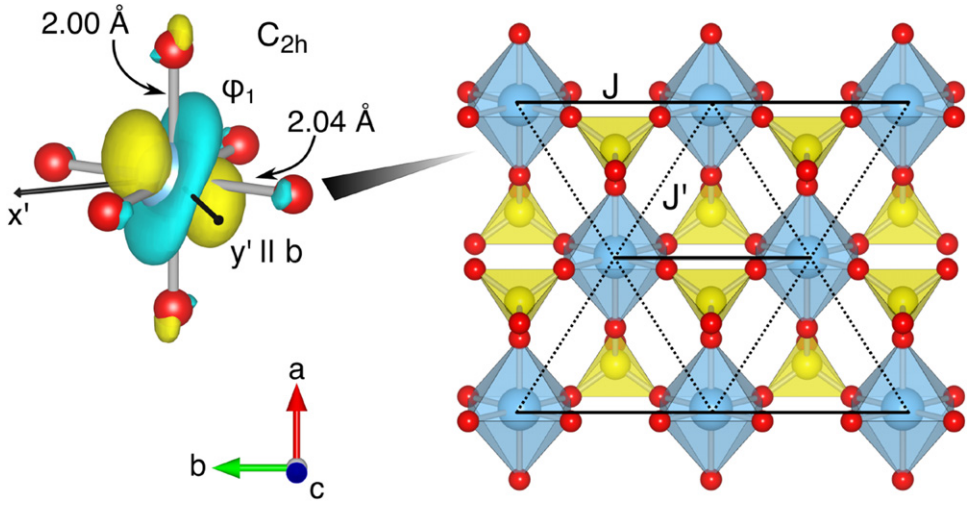

Figure 1. (Right) The structure of $KTi(SO_4)_2$ viewed along the c^* axis. The TiO_6 octahedra are displayed in blue and the SO_4 tetrahedra in yellow. The interplane K^+ ions have been left out for clarity. The anisotropic triangular magnetic lattice has been plotted on top of the structure, with J represented as solid black lines along $\langle 010 \rangle$ and J' as dashed lines along $\langle 110 \rangle$, respectively. (left) A magnified view of a single TiO_6 octahedron. The isosurface represents the Ti^{3+} ground-state Wannier orbital φ_1 drawn at arbitrary probability, and the black arrows denote the $x'$and y'directions in the rotated local coordinate frame. The dominant superexchange pathway proceeds through the equatorial oxygens, lying at the Ti–O distance 2.044(1) Å. The figure was obtained using the VESTA software [20].

arising from the single unpaired electron in the d-shell of Ti^{3+}. $KTi(SO_4)_2$ is isomorphous with the naturally occurring mineral yavapaiite, $KFe(SO_4)_2$, which crystallizes in the monoclinic $C2/m$ space group [22]. The structure consists of sheets of octahedrally coordinated Ti^{3+} ions bridged by $(SO_4)^{2-}$ ions to form an anisotropic triangular lattice in the ab plane. The Ti–Ti nearest-neighbour distances along the $\langle 010 \rangle$ and $\langle 110 \rangle$ directions are 5.24 Å and 4.88 Å, respectively, with the corresponding exchanges labelled J and J' (figure 1). Because superexchange between neighbouring Ti^{3+} proceeds along a Ti–O–S–O–Ti pathway in both cases, J and J' are expected to be small. Furthermore, because each nearest neighbour bond contains an inversion centre, no Dzyaloshinskii–Moriya terms are allowed (unlike in Cs_2CuCl_4). The triangular lattice $[Ti(SO_4)_2]^-$ sheets are well separated by K^+ ions along the c direction, with the interlayer distance corresponding to 7.74 Å. In [21], the magnetic susceptibility $\chi(T)$ of $KTi(SO_4)_2$ is found to show a broad shoulder indicating short range correlations at 7 K, followed by a sharp Curie-like increase, possibly caused by a paramagnetic impurity, at lower temperatures. Based on the small Curie constant (and hence magnetic moment) attained from fits to the high temperature data, it was speculated that the Ti^{3+} moment possesses an Ising anisotropy, as has been observed in the fully hydrated alum $Cs[Ti:Al](SO_4)_2 \cdot 12H_2O$, where $g_{\parallel} = 1.166$ and $g_{\perp} = 0.230$ [23].

In this paper, we will show that $KTi(SO_4)_2$ is in fact an excellent realization of the AQHC. This change in interpretation has been made possible by the availability of higher quality samples synthesized by a new hydrothermal route. Standard analysis of the magnetic susceptibility yields nearly the full spin-only moment for $S = 1/2$, which may be understood in the context of an unusual orbital ground state revealed by DFT calculations. This ground state also explains the strong one-dimensionality of the magnetism, confirmed by fits to series expansion results for the QHAT and exact diagonalizations for the the isolated AQHC. Finally, time-of-flight neutron spectroscopy results are in near perfect agreement with the exact two- and four-spinon cross section for the AQHC, despite the use of a powder sample.

2. Synthesis and magnetic interactions

We begin by briefly discussing the sample synthesis: the literature route to $KTi(SO_4)_2$ involves vacuum dehydration of a stoichiometric solution of $Ti_2(SO_4)_3$ and K_2SO_4, followed by regrinding and annealing [21]. As stated previously, this protocol appears to also generate a large paramagnetic impurity and/or lattice defects. To prepare the present samples of $KTi(SO_4)_2$, we instead begin with a solution of $Ti_2(SO_4)_3$ and K_2SO_4 (molar ratio 3.5: 1) in H_2SO_4 (1.9 mol dm^3)[6]. The solution is enclosed in a 35 ml thick-walled teflon-stoppered pyrex tubes (Ace glass) and heated to 155 °C for 48 h, before slowly cooling to room temperature over 24 h. Small ($\sim$0.1 mm^3) crystals of $KTi(SO_4)_2$ are found on the sides of the vessel alongside a moderate amount of non-magnetic TiO_2 (anatase) powder, which may be partly removed by washing. X-ray diffraction confirms the

[6] The composition of the starting solution and the reaction conditions are similar to those used in the synthesis of the monohydrate $KTi(SO_4)_2 \cdot H_2O$, another low dimensional magnetic system [24].

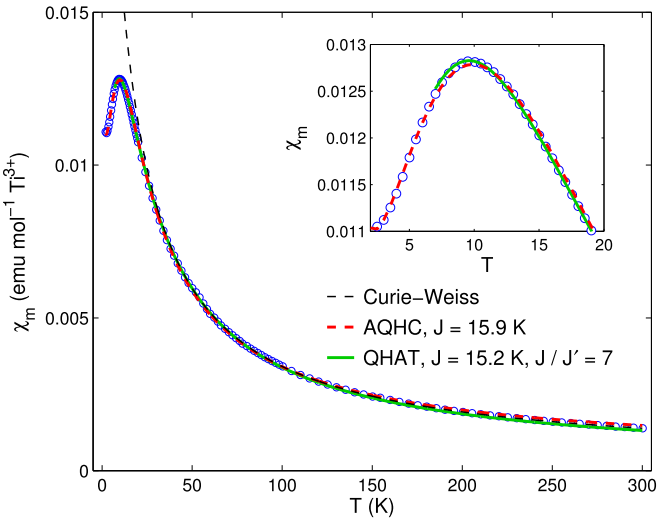

Figure 2. Magnetic susceptibility $\chi_m(T)$ of Ti-yavapaiite. The experimental data recorded at 1000 Oe is plotted with blue circles, while the fits to the Curie–Weiss law, the AQHC, and the QHAT are indicated by black dashed, red dashed, and green solid lines, respectively. The latter is only plotted down to 8 $K \simeq 0.8 T_p$ due to the divergence of the [5,5] Padé approximant below this temperature. The inset shows a magnified region around the low temperature peak.

monoclinic space group of $KTi(SO_4)_2$, and yields room temperature lattice parameters $a = 8.2894(3)$ Å, $b = 5.2257(2)$ Å, $c = 7.8441(3)$ Å, and $\beta = 94.645(2)°$. Refinements of neutron diffraction data taken at 2 K on the D1A diffractomer at the Institut Laue–Langevin (ILL) (see figure S1 in the supplementary material) indicate that a and c contract from their room temperature values to 8.2402(2) Å and 7.7678(1) Å, respectively. More surprisingly, b shows a slight expansion to 5.23511(9) Å. The phase fraction of anatase is estimated by the same refinement to be ∼10 %.

A few clusters of crystals (in total 126.9 mg) were selected for magnetic susceptibility measurements, carried out in an applied magnetic field $H = 1000$ Oe using a Quantum Design MPMS-5 magnetometer; the temperature dependence of the molar susceptibility $\chi_m(T)$ is shown in figure 2. At high temperature, $\chi_m(T)$ follows the Curie–Weiss law $\chi_m(T) = C/(T - \theta_{CW}) + \chi_0$, where $C = N_A \mu_{eff}^2/(3k_B)$ and θ_{CW} are, respectively, the Curie and the Weiss constants, and χ_0 is a T-independent background. Fitting in the temperature range 50 − 300 K yields values of $\theta_{CW} = -11(2)$ K and an effective magnetic moment $\mu_{eff} = 1.68(2)\ \mu_B$, indicating weak antiferromagnetic couplings and a nearly full $S = 1/2$ spin-only moment [$g_{eff} = 1.94(3)$]. The relatively large background $\chi_0 = 3 \times 10^{-4}$ originates from the core diamagnetism of $KTi(SO_4)_2$ and the plastic sample holder. At lower temperatures, a broad, symmetric maximum characteristic of short range order appears around $T_p = 10$ K (figure 2(inset)). No signs of either a large Curie tail, as seen in [21], nor a magnetic long range ordering anomaly are observed.

Based on the arrangement of Ti^{3+} ions in $KTi(SO_4)_2$, the most obvious starting point to fit $\chi_m(T)$ is the QHAT, described by the Hamiltonian $\mathcal{H}_{QHAT} = J \sum_{\langle i,j \rangle} \mathbf{S}_i \cdot \mathbf{S}_j + J' \sum_{\langle\langle i,j \rangle\rangle} \mathbf{S}_i \cdot \mathbf{S}_j$, where $\mathbf{S}_{i,j}$ are the Heisenberg spin operators on pairs sites i, j within (first term) and between (second term) chains. To this end, we calculate the Padé approximants of the 10th order high-T series expansion derived for $\mathcal{H}_{QHAT}$ by Zheng *et al* [25] using the continued fraction quotient-difference algorithm [26]. All approximants are found to diverge at temperatures below $T \simeq 0.8\ T_p$ for $J/J' > 5$, which is therefore used as the lower limit for the fitting range. Remarkably, the best fit ($\chi^2 = 6.0$) to the experimental curve is achieved for $J = 15.2$ K and $J/J' = 9(1)$, very close to the isolated one-dimensional chain limit. Indeed, decreasing J/J' to 6 leads to an appreciable asymmetry in the peak, reflected by a poorer $\chi^2 = 18.0$. Given the large ratio of J/J', we also attempt a fit to exact diagonalization results[7] for the isolated AQHC ($J' = 0$) model with a small paramagnetic tail, yielding the red curve in figure 2. While $\chi^2 = 40.2$ is worse than for both QHAT fits, the peak (in particular its symmetry) at T_p is nonetheless well described. We will return to the role of the interchain coupling in the context of our neutron scattering results further on in this manuscript.

3. Orbital ground state and superexchange

To understand the large measured moment and apparent one-dimensionality of the magnetism in $KTi(SO_4)_2$, we return to its structure, and in particular, the geometry of the Ti^{3+} octahedra. In d^1 compounds, the interplay

[7] The simulation was carried out using the ALPS package [27] on a chain of 20 spins with periodic boundary conditions.

of crystal field terms and spin–orbit coupling are crucially important for determining the single-ion magnetic properties. For perfect octahedral coordination (point group O_h), the ^2D free ion state is split into the usual set of t_{2g} and e_g levels, with the lone electron populating the former. The three-fold degeneracy of the crystal field ground state is lifted by LS-coupling to an effective $\mathbf{L} = -1$ orbital momentum, resulting in a non-Kramers pair of doublets in the ground state, both with $g = \langle L + 2S \rangle = 0$ [23]. Lowering the symmetry to tetragonal (D_{4h}), the symmetry and magnitude of the magnetic moment become dependent on the sign and magnitude, δ, of the tetragonal distortion; when the octahedron is axially compressed ($\delta < 0$), the orbital ground state is based on the d_{xy} orbital, which yields a Kramers doublet ground state with $g = 2$, i.e. Heisenberg spins. The nearly tetragonal (C_{2h}) local environment of Ti^{3+} in $KTi(SO_4)_2$ indeed appears to fulfil this condition, with two short axial and four long equatorial Ti–O distances (2.000(1) Å versus 2.044(1) Å from neutron diffraction) and O–Ti–O angles close to 90° (figure 1). The resulting d_{xy} orbital order is anticipated to produce dominant exchange along the b-direction, along which the Ti–O orbital overlap is large. Both the observation of a nearly full $S = 1/2$ moment and the one-dimensionality thus appear to be accounted for.

This simple picture is challenged by density-functional (DFT) calculations performed in the local density approximation (LDA) [28] using the FPLO code [29]. The orbital energies are extracted by fitting Wannier functions to the resulting d-bands, which comprise the t_{2g} states around the Fermi level and the e_g states 2 eV higher in energy (figure S3). Using the orthogonalized local coordinate frame with x, y, and z directed along the Ti–O bonds, we find $\varepsilon_{xy} = 0.203$ eV and $\varepsilon_{yz} = \varepsilon_{xz} = 0.135$ eV. While this splitting is compatible with the crystal-field scheme for D_{4h} described above, the orbitals are ordered contrary to the expectation for $\delta < 0$. Before addressing this discrepancy, we consider the effect of lowering the site symmetry to C_{2h}, which entails an additional small splitting between the d_{yz} and d_{xz} states. This splitting becomes visible when the local $y \rightarrow y'$ axis is directed along the two-fold rotation axis between two adjacent oxygen atoms in the xy plane. In the new $x'y'z$ coordinate frame, effectively the original frame with x and y axes turned by 45° (figure 1), the d_{xy} orbital has $(x')^2 - (y')^2$ symmetry, and the orbital energies become $\varepsilon_{(x')^2-(y')^2} = 0.216$, $\varepsilon_{y'z} = 0.112$, and $\varepsilon_{x'z} = 0.083$ eV.

The result that $\varepsilon_{x'z} < \varepsilon_{y'z}$ is again at odds with the geometry of the Ti^{3+} octahedron, which implies $\varepsilon_{x'z} > \varepsilon_{y'z}$. This arrangement is expected from the scissor-like distortion of the O atoms in the xy plane, where the O–Ti–O angles are 88° and 92°, respectively. The closer proximity of the O^{2-} ions to x', which bisects the smaller angle, then suggests $\varepsilon_{x'z} > \varepsilon_{y'z}$. Taking this and the unexpectedly high energy of the $(x')^2 - (y')^2$ orbital into account, it appears that the ions beyond the nearest-neighbour oxygens play the decisive role in the ordering of the t_{2g} orbitals. This is perhaps not surprising given the small magnitude of the distortion of the Ti^{3+} octahedron; the difference between axial and equatorial Ti–O bond lengths is only 0.2%. In the present case, the $d_{x'z}$-orbital may be stabilized by the positively charged K^+ ions along the x'-direction, located at a Ti–K distance of 3.88 Å. It may also be envisaged that the second-neighbour oxygens within the SO_4 tetrahedra contribute; these are more remote from Ti^{3+} along the x'-direction (Ti–O2 distance of 4.30 Å) than along the y'-direction (Ti–O1 distance of 3.45 Å and Ti–O3 distance of 4.09 Å). While these oxygens may also be responsible for the high energy of the $(x')^2 - (y')^2$ orbital in energy, this is less evident.

To investigate the orbital ground state of Ti^{3+} in $KTi(SO_4)_2$ under more realistic conditions, we extend the above calculations by adding a Hubbard U at the mean-field level (LSDA+U). Occupations of d-orbitals are varied as to minimize the total energy under the presence of the Hubbard term [8]. These calculations yield an insulating state with a band gap of 2.3 eV and a ground-state orbital wave-function $|\varphi_1\rangle = 1/\sqrt{5}\,(|(x')^2 - (y')^2\rangle + 2|x'z\rangle)$, obtained by diagonalizing the d-orbital occupation matrix.

We now perform the Wannier fit to the original LDA bands using an orthonormal basis containing the $|\varphi_1\rangle$ orbital (figure 1) together with $|\varphi_2\rangle = 1/\sqrt{5}\,(2|(x')^2 - (y')^2\rangle - |x'z\rangle)$, $|y'z\rangle$, and the two e_g states. The energies of the t_{2g} orbitals become $\varepsilon_{\varphi 1} = 0.064$, $\varepsilon_{y'z} = 0.112$, and $\varepsilon_{\varphi 2} = 0.235$ eV; the $|\varphi_1\rangle$ orbital indeed has the lowest energy at the LDA level (figure S3). The nearest-neighbour Ti–Ti hoppings of this state corresponding to the pathways for the exchange couplings J and J' are $t = -0.045$ eV and $t' = 0.023$ eV, respectively. Using the full five-band tight-binding model and adding an effective Hubbard $U_{\rm eff} = 4$ eV and Hund's coupling $\mathcal{J}_{\rm eff} = 1$ eV, we compute exchange couplings from the Kugel–Khomskii model [31, 32] and arrive at $J = 18.3$ K and $J' = 5.1$ K ($J/J' = 3.6$) in reasonable agreement with the susceptibility fits. Alternatively, we obtain $J = 16$ K and $J' = 7$ K ($J/J' = 2.3$) from LSDA+U total energies of ferromagnetic and antiferromagnetic spin configurations (the so-called supercell method). However, these LSDA+U-based values appear to be strongly dependent on the choice of the Hubbard U and on the double-counting correction method in LSDA+U.

$KTi(SO_4)_2$ may thus be said to feature a well-defined but rather unexpected orbital state described by $|\varphi_1\rangle$, which is triggered by the weak crystal-field splitting of the t_{2g} states. This splitting is not consistent with the local distortion of the TiO_6 octahedron and reflects a complex interplay of ionic charges surrounding the Ti^{3+} ion in the crystal structure. A similar inversion of the orbital energies with respect to crystal-field predictions for nearest-neighbour oxygens has also recently been demonstrated in the iridate compound Sr_2IrO_4 [33]. Finally,

[8] We used the on-site Hubbard repulsion $U_d = 4$ eV and Hund's exchange $J_d = 1$ eV following our recent study of $KTi(SO_4)_2 \cdot 2H_2O$ in [30].

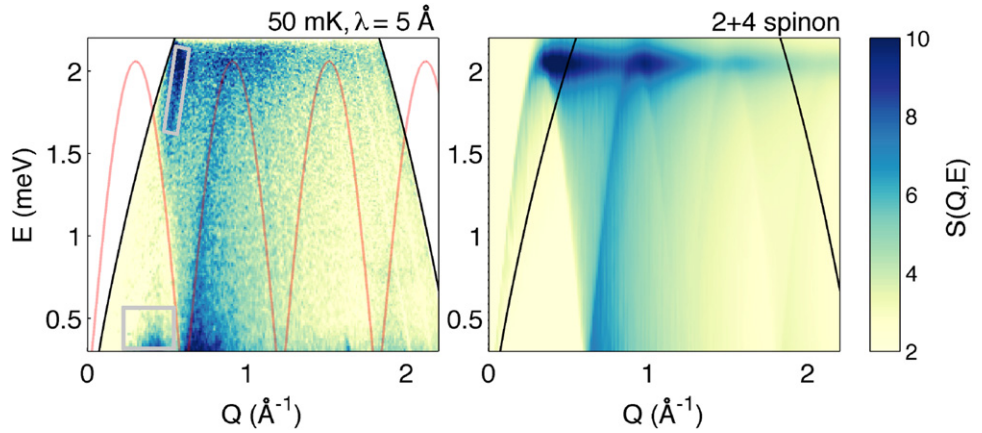

Figure 3. (a) The background-subtracted experimental $S(Q, E)$ of $KTi(SO_4)_2$ measured at 50 mK on the IN5 spectrometer (ILL) using 5 Å neutrons. The grey bar and grey square correspond to the position of spurious features due to scattering from the beam-stop, while the red line corresponds to the lower bound of the two-spinon continuum $E_s(Q)$ (see text). (b) The powder-averaged two- and four-spinon dynamical scattering function $S(Q, E)^{\mathrm{pow}}_{2+4}$; qualitative agreement with (a) is excellent for $J = 15.2$ K. The black line marks the boundary of the experimental (Q, E) window at $\lambda_i = 5$ Å.

the ground-state orbital yields quasi-one-dimensional magnetism with the dominant exchange along the b direction, thus revealing the origin of the behaviour observed in our magnetic susceptibility measurements. We will confirm that the b-axis is the one-dimensional axis in the following section.

4. Magnetic excitations

To address the unsettled question of the interchain couplings (and more generally, the magnetic excitations) in $KTi(SO_4)_2$, we carried out a time-of-flight neutron scattering on the IN5 spectrometer at the ILL. Approximately 10 g of polycrystalline $KTi(SO_4)_2$ (the same sample as used for neutron diffraction on D1A) were loaded in a cylindrical Cu can of diameter 11 mm, which was connected to the end of an ILL-built dilution refrigerator with a base temperature of 50 mK. Around 1 bar (at 298 K) of ^{4}He exchange gas was admitted into the can to thermalize the sample at sub-Kelvin temperatures. Given the energy scale extracted from the fits to $\chi_{\mathrm{m}}(T)$, wavelengths of $\lambda_i = 3$ Å$(E_i = 9.09$ meV) and 5 Å$(E_i = 3.27$ meV) were selected by a pair of counter-rotating disk choppers. For both wavelengths, the choppers were spun at 17000 rpm to yield full-width half-maximum E-resolutions at the elastic line of 0.31 meV and 0.07 meV, respectively. The data were corrected for detector efficiency using a vanadium standard, the E-dependent self-attenuation of the sample, as well as background from the sample environment. Unfortunately, it was not possible to fully subtract a component arising from the beam stop, which manifests itself as strong spurious scattering at small angle in the entire energy transfer window for both wavelengths (figure 3(a))[9].

The dynamical scattering function $S(Q, E = \hbar\omega)$ at 50 mK for $\lambda_i = 5$ Å is shown in figure 3(a). A clear branch of excitations is observed dispersing from the vicinity of the antiferromagnetic position $(0\frac{1}{2}0)$ up to $\sim$2 meV. Upon initial inspection, the powder averaging renders it difficult to distinguish whether this represents conventional magnons or a spinon continuum. However, the sharp onset of the scattering, particularly at small E (figure 4(a)), can be associated with a powder averaged one-dimensional dispersion. Furthermore, the lower bound of the spinon continuum is expected to be found at $E_s(Q) = \frac{\pi}{2} J \cos(Q_x)$, where Q_x is the component of the wave-vector transfer Q along the chain direction. Choosing $J = 1.31$ meV $= 15.2$ K and $Q_x \,||\, b^*$, as inferred from our fits to $\chi_{\mathrm{m}}(T)$ and electronic structure calculations, we find excellent agreement with the observed dispersion. The semi-classical spin wave solution, on the other hand, indicates a zone-boundary energy of $J = 1.32$ meV, clearly inconsistent with the data. It also predicts an absence of scattering beyond the dispersion maximum, which a Q-integrated slice of the 3 Å data verifies is not the case (figure 4(f)).

We now attempt to put our claim that the observed scattering represents a spinon continuum on a more quantitative footing. The two- and four-spinon dynamical structure factor $S(Q, E)_{2+4}$ for the QHCA has been obtained exactly by Caux and Hagemans [6] from an algebraic treatment based on the observation that even-spinon states are eigenstates of the AQHC Hamiltonian. Using this result as a starting point, spherical (powder) averaging was carried out assuming no dispersion or modulation of the intensity perpendicular to Q_x. To achieve

[9] This issue has since been resolved.

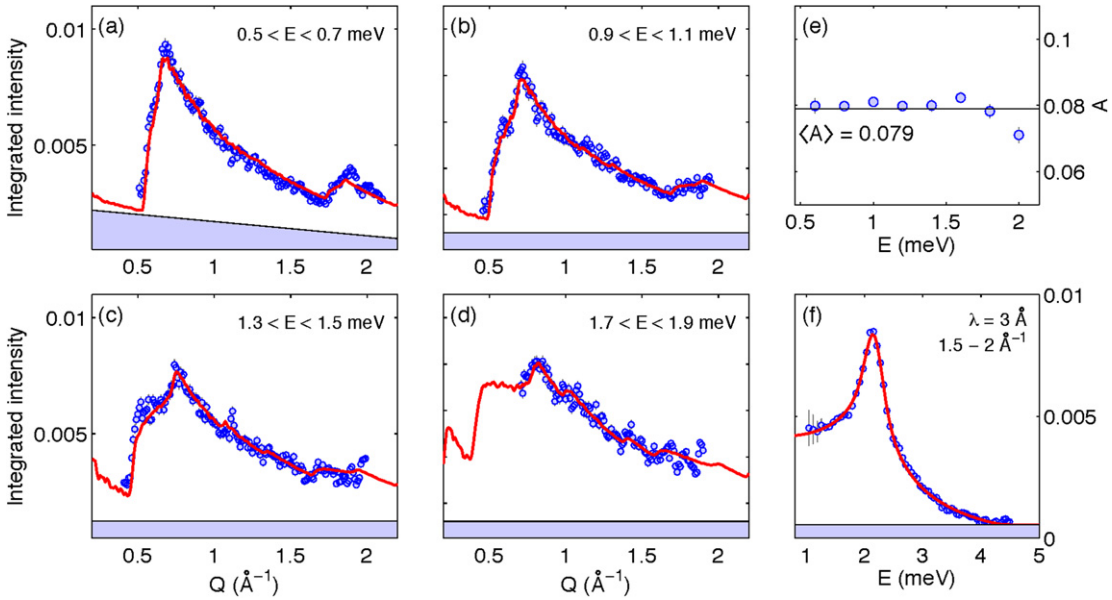

Figure 4. (a)–(d) E-integrated strips at selected energies for $\lambda_i = 5$ Å. In each, the fit to $S(Q, E)^{\mathrm{pow}}_{2+4}$ is indicated by a solid red line, and the background by the shaded region. (e) The E-dependence of the fitting amplitude. The black line represents the average amplitude $\langle A \rangle = 0.079$, from which the highest E points deviates by around 10%. (f) A Q-integrated slice taken from the $\lambda_i = 3$ Å data. Again, the fit to $S(Q, E)^{\mathrm{pow}}_{2+4}$, here convoluted with an E-dependent resolution, is indicated by a solid red line.

a uniform sampling on the constant-Q sphere, random Cartesian coordinates were selected from a Gaussian distribution and normalized to the sphere radius. The $S(Q, E)^{\mathrm{pow}}_{2+4}$ resulting from this procedure is shown in figure 3(b). The Q-dependence of the experimental $S(Q, E)$ was extracted by integrating over a series of 0.2 meV wide strips between $E = 0.5$ and 2.1 meV (figures 4(a)–(d)). These strips were then fitted to the corresponding section of the powder-averaged $S(Q, E)^{\mathrm{pow}}_{2+4}$; for each strip, the background and amplitude $A(E)$ were adjustable parameters, while J was considered a global parameter. Regions in Q contaminated by scattering from the beam-stop were not included in the fitting range. The fits for selected energies up to 2.1 meV $\sim$ max E_s are shown in figures 4(a)–(d), with $A(E)$ given in figure 4(e). Excellent agreement between experiment and theory is found for all strips using $J = 1.32(2)$ meV $= 15.3(2)$ K. Furthermore, $A(E)$ is broadly consistent across the full energy range, but shows a $\sim$10% drop from its average value $\langle A \rangle = 0.079$ for the highest energy strip (figure 4(e)). Although a small J'could explain this small deviation [18], we will show that the likeliest explanation is the imperfect correction of the experimental data.

To verify the robustness of the AQHC with respect to our fits, we turn to the E-dependent strip through the 3 Å data-set discussed above (figure 4(f)). As the scattering up to $\sim$1 Å^{-1} contains a strong contribution from the background, we integrate $S(Q, E)$ over the range 1.5–2.0 Å^{-1}. This range furthermore covers $Q \simeq 1.7$ Å^{-1}, where J' is expected to cause a large redistribution of intensity from the powder-averaging of the inter-chain dispersion. In order to fit $S(Q, E)^{\mathrm{pow}}_{2+4}$ to the experimental data, we convolute it pixel-by-pixel with an E-dependent resolution calculated from the expression given in [34]. Again, the agreement with the model is nearly perfect (figure 4(f)) for $J = 1.38(2)$ meV $= 16.0(2)$ K, close to the value extracted from our 5 Å dataset and susceptibility fit. This indicates that slight variation in $A(E)$ observed at the longer neutron wavelength $\lambda = 5$ Å is probably an experimental artefact, with the self-attenuation correction, which neglects the absorption in the walls of the Cu can, the most likely source of the error. Based on the above, as well as the fact that no asymmetry is observed in the dispersion, it thus appears that $KTi(SO_4)_2$ is close to an ideal realization of the AQHC, fulfilling the condition $J \gg J'$.

Finally, we search for evidence of magnetic order below 1.8 K by comparing our 50 mK data to higher temperature datasets; subtraction of datasets collected in the range 1.3–10 K do not result in any systematic changes in the elastic scattering consistent with magnetic order (see figure S2, supplemental material). Using the intensity of the (001) nuclear Bragg peak, the statistical error of our data, and assuming collinear Néel order propagating with $\mathbf{k} = (0\frac{1}{2}0)$, we estimate an upper limit for the ordered moment of $\mu_o \sim 0.1\ \mu_B$ for any magnetic moment direction. Despite the small magnitude of this estimate, magnetic order cannot be excluded in $KTi(SO_4)_2$; in fact, strongly suppressed ordered moments (and Néel temperatures, T_N) are a general feature of one-dimensional materials. Indeed, several quasi-1D systems, including Sr_2CuO_3 and Ca_2CuO_3, show $\mu_o < 0.1\ \mu_B$ [35]. The small ordered moments and Néel temperatures can be partly understood in the context of

quantum field theory calculations, which yield $\mu_o \sim C_1\sqrt{J_c/J}$, where J_c is an unfrustrated interchain coupling, and $T_N \sim C_2 J_c$ (ignoring logarithmic corrections). C_1 and C_2 are constants, and correspond to ~1 and ~0.8 for a cubic arrangement of spin chains [36, 37]. Similar calculations on stacked anisotropic triangular planes (as in $KTi(SO_4)_2$) show that the latter relation still holds, but that the constant C_2 is reduced by a factor ~2; this is presumably because the frustration within the planes reduces the effective number of nearest neighbour chains from four (in the cubic case) to two. The reduction in C_1 should correspondingly be $\sqrt{2}$; from this, we may estimate an interchain coupling between adjacent planes of $J_c < 0.02J = 0.3$ K, and thus $T_N < 0.4$ K [38]. This is consistent with the $J_c = 0.05$ K ($J/J_c \simeq 300$) extracted from our DFT calculations. Regardless of the presence or absence of magnetic order in $KTi(SO_4)_2$, the excitation spectrum is expected to remain largely unchanged except at very low energies <0.25 meV, where transverse spin waves and a gapped longitudinal spin-wave mode may occur [39–43].

5. Conclusion

To conclude, the recent preparation of high-quality samples of the anhydrous alum $KTi(SO_4)_2$ have allowed us to re-evaluate its magnetic properties. Fits to both magnetic susceptibility and inelastic neutron scattering data indicate that it is an excellent realization of the AQHC, with $J = 15.3(2)$ K $= 1.32(2)$ meV, and $g \simeq 2$. These properties appear to arise from an unusual orbital order on the Ti^{3+} site, which results in moderate antiferromagnetic superexchange along the crystallographic *b*-direction and weak exchange along other directions. A few points remain to to be clarified, however, most prominently the possible presence of magnetic order at $T < 0.4$ K due to interchain couplings. This problem is most appropriately dealt with by inelastic or polarized neutron scattering at lower energies than presented here, as well as muon spin rotation.

Acknowledgments

We are grateful to S T Bramwell, M Mourigal, and A R Wildes for useful discussions and J -S Caux for helpful comments and for supplying the dynamical structure factor data. The experimental work was supported by the Swiss National Science foundation and its Synergia network Mott Physics Beyond the Heisenberg Model. AT was funded by the Federal Ministry for Education and Research through the Sofja Kovalevskaya award of the Alexander von Humboldt Foundation. DK acknowledges funding by the Deutsche Forschungsgemeinschaft (DFG) within Forschergruppe (FOR) 1346.

References

[1] Sutherland W 2004 *Beautiful Models: 70 Years of Exactly Solved Quantum Many-Body Problems* (Singapore: World Scientific)
[2] Bethe H 1931 Zur Theorie der Metalle I. Eigenwerte and Eigenfunktionen der linearen Atomkette *Z. Phys.* A **71** 205
[3] Hulthén L 1938 Über das Austauschproblem eines Kristalles *Ark. Mat. Astron. Fys.* **26A** 1
[4] Cloizeaux J des and Pearson J J 1962 Spin-wave spectrum of antiferromagnetic linear chain *Phys. Rev.* **128** 2131
[5] Yamada T 1969 Fermi-liquid theory of linear antiferromagnetic chains *Prog. Theor. Phys.* **41** 880
[6] Caux J-S and Hagemans R 2006 The four-spinon dynamical structure factor of the Heisenberg chain *J. Stat. Mech.* **12** 12013
[7] Walters A C, Perring T G, Caux J-S, Savici A T, Gu G D, Lee C-C, Ku W and Zaliznyak I A 2009 Effect of covalent bonding on magnetism and the missing neutron intensity in copper oxide compounds *Nat. Phys.* **5** 867–72
[8] Mourigal M, Enderle M, Kloepperpieper A, Caux J-S, Stunault A and Rønnow H M 2013 Fractional spinon excitations in the quantum Heisenberg antiferromagnetic chain *Nat. Phys.* **9** 435–41
[9] Lake B, Tennant D A, Caux J-S, Barthel T, Schollwock U, Nagler S E and Frost C D 2013 Multispinon continua at zero and finite temperature in a near-ideal Heisenberg chain *Phys. Rev. Lett.* **111** 137205
[10] Stone M B, Reich D H, Broholm C, Lefmann K, Rischel C, Landee C P and Turnbull M M 2003 Extended quantum critical phase in a magnetized spin-1/2 antiferromagnetic chain *Phys. Rev. Lett.* **91** 037205
[11] Lake B, Tennant D A, Frost C D and Nagler S E 2005 Quantum criticality and universal scaling of a quantum antiferromagnet *Nat. Mater.* **4** 329–34
[12] Weihong Z, McKenzie R H and Singh R R P 1999 Phase diagram for a class of spin-1/2 Heisenberg models interpolating between the square-lattice, the triangular-lattice, and the linear-chain limits *Phys. Rev.* B **59** 14367–75
[13] Yunoki S and Sorella S 2006 Two spin liquid phases in the spatially anisotropic triangular Heisenberg model *Phys. Rev.* B **74** 014408
[14] Starykh O A and Balents L 2007 Ordering in spatially anisotropic triangular antiferromagnets *Phys. Rev. Lett.* **98** 077205
[15] Carlin R L, Burriel R, Palacio F, Carlin R A, Keij S F and Carnegie D W 1985 Linear-chain antiferromagnetic interactions in Cs_2CuCl_4 *J. Appl. Phys.* **57** 3351–2
[16] Coldea R, Tennant D A, Cowley R A, McMorrow D F, Dorner B and Tylczynski Z 1996 Neutron scattering study of the magnetic structure of Cs_2CuCl_4 *J. Phys.: Condens. Matter* **8** 7473–91
[17] Coldea R, Tennant D A and Tylczynski Z 2003 Extended scattering continua characteristic of spin fractionalization in the two-dimensional frustrated quantum magnet Cs_2CuCl_4 observed by neutron scattering *Phys. Rev.* B **68** 134424
[18] Kohno M, Starykh O A and Balents L 2007 Spinons and triplons in spatially anisotropic frustrated antiferromagnets *Nat. Phys.* **3** 790–5
[19] Ono T, Tanaka H, Katori H A, Ishikawa F, Mitamura H and Goto T 2003 Magnetization plateau in the frustrated quantum spin system Cs2CuBr4 *Phys. Rev.* B **67** 104431

[20] Momma K and Izumi F 2011 Vesta 3 for three-dimensional visualization of crystal, volumetric and morphology data *J. Appl. Crystallogr.* **44** 1272–6
[21] Bramwell S T, Carling S G, Harding C J, Harris K D M, Kariuki B M, Nixon L and Parkin I P 1996 The anhydrous alums as model triangular-lattice magnets *J. Phys.: Condens. Matter* **8** L123
[22] Graeber E J and Rosenzweig W 1971 Crystal-structures of yavapaiite, $KFe(SO_4)_2$, and goldichite, $KFe(SO_4)_2.4H_2O$ *Am. Mineral.* **56** 1917
[23] Dionne G F and MacKinnon J A 1968 Origin of crystal field in Ti^{3+}-substituted alums *Phys. Rev.* **172** 325
[24] Nilsen G J, Rønnow H M, Läuchli A M, Fabbiani F P A, Sanchez-Benitez J, Kamenev K V and Harrison A 2008 A new realisation of the $s = 1/2$ frustrated chain antiferromagnet *Chem. Mater.* **20** 8–10
[25] Zheng W, Singh R R P, McKenzie R H and Coldea R 2005 Temperature dependence of the magnetic susceptibility for triangular-lattice antiferromagnets with spatially anisotropic exchange constants *Phys. Rev.* B **71** 134422
[26] McCabe J H 1983 The quotient-difference algorithm and the Padé table: an alternative form and a general continued fraction *Math. Comput.* **41** 183
[27] Bauer B *et al* 2011 The ALPS project release 2.0: open source software for strongly correlated systems *J. Stat. Mech.* **2011**
[28] Perdew J P and Wang Y 1992 Accurate and simple analytic representation of the electron–gas correlation energy *Phys. Rev.* B **45** 13244–9
[29] Koepernik K and Eschrig H 1999 Full-potential nonorthogonal local-orbital minimum-basis band-structure scheme *Phys. Rev.* B **59** 1743–57
[30] Kasinathan D, Koepernik K, Janson O, Nilsen G J, Piatek J O, Rønnow H M and Rosner H 2013 Electronic structure of $KTi(SO_4)_2 \cdot H_2O$: an $S = 1/2$ frustrated chain antiferromagnet *Phys. Rev.* B **88** 224410
[31] Mazurenko V V, Mila F and Anisimov V I 2006 Electronic structure and exchange interactions of $Na_2V_3O_7$ *Phys. Rev.* B **73** 014418
[32] Tsirlin A A, Janson O and Rosner H 2011 Unusual ferromagnetic superexchange in $CdVO_3$: the role of Cd *Phys. Rev.* B **84** 144429
[33] Bogdanov N A, Katukuri V M, Romhanyi J, Yushankhai V, Kataev V, Buchner B, Van Den Brink J and Hozoi L 2015 Orbital reconstruction in nonpolar tetravalent transition-metal oxide layers *Nat. Commun.* **6** 7306
[34] Lechner R E 1990 Optimization of a multi-disk chopper spectrometer for cold neutron scattering experiments *Int. Collaboration on Advanced Neutron Sources* (*JAERI, Tsukuba, October 22–26, 1990*) ed M Misawa *et al*
[35] Kojima K M *et al* 1997 Reduction of ordered moment and Néel temperature of quasi-one-dimensional antiferromagnets Sr_2CuO_3 and Ca_2CuO_3 *Phys. Rev. Lett.* **78** 1787–90
[36] Schulz H J 1996 Dynamics of coupled quantum spin chains *Phys. Rev. Lett.* **77** 2790–3
[37] Irkhin V Y and Katanin A A 2000 Calculation of Neel temperature for $S = 1/2$ Heisenberg quasi-one-dimensional antiferromagnets *Phys. Rev.* B **61** 6757–64
[38] Bocquet M, Essler F H L, Tsvelik A M and Gogolin A O 2001 Finite-temperature dynamical magnetic susceptibility of quasi-one-dimensional frustrated spin-1/2 Heisenberg antiferromagnets *Phys. Rev.* B **64** 094425
[39] Essler F H L, Tsvelik A M and Delfino G 1997 Quasi-one-dimensional spin-1/2 Heisenberg magnets in their ordered phase: correlation functions *Phys. Rev.* B **56** 11001–13
[40] Lake B, Tennant D A and Nagler S E 2000 Novel longitudinal mode in the coupled quantum chain compound $KCuF_3$ *Phys. Rev. Lett.* **85** 832–5
[41] Lake B, Tennant D A and Nagler S E 2005 Longitudinal magnetic dynamics and dimensional crossover in the quasi-one-dimensional spin-1/2 Heisenberg antiferromagnet $KCuF_3$ *Phys. Rev.* B **71** 134412
[42] Zheludev A, Kakurai K, Masuda T, Uchinokura K and Nakajima K 2002 Dominance of the excitation continuum in the longitudinal spectrum of weakly coupled Heisenberg $S = 1/2$ chains *Phys. Rev. Lett.* **89** 197205
[43] Zheludev A, Kenzelmann M, Raymond S, Masuda T, Uchinokura K and Lee S H 2002 Spin dynamics in the quasi-one-dimensional $S = 1/2$ antiferromagnet $BaCu_2Si_2O_7$ *Phys. Rev.* B **65** 014402